Structural- and Optical- Properties Analysis of Single Crystalline Hematite (α-Fe_2O_3) Nanocubes Prepared by One-Pot Hydrothermal Approach

Nur Maisarah Abdul Rashid[a], Choonyian Haw[a], Weesiong Chiu[a,*], Noor Hamizah Khanis[a], Aliff Rohaizad[a], Saadah Abdul Rahman[a,*], PoiSim Khiew[b]

[a]Low Dimensional Materials Research Centre, Department of Physics, University of Malaya, 50603 Kuala Lumpur, Malaysia

[b]Department of Chemical Engineering, Faculty of Engineering, University of Nottingham Malaysia Campus, Jalan Broga, 43500 Semenyih, Selangor Darul Ehsan, Malaysia

**Correspondence should be addressed to Chiu Wee Siong; w.s.chiu@um.edu.my and Saadah Abdul Rahman: saadah@um.edu.my*

Abstract

High quality single crystal hematite (α-Fe_2O_3) nanocubes with average dimensions of 40 nm were successfully synthesized by a facile one-pot hydrothermal method. Systematic analyses were performed to investigate the morphological-, structural- and optical-properties of the as-synthesized α-Fe_2O_3 nanocubes. Continuous formation and hourly monitored towards proper arrangement of single crystal α-Fe_2O_3 nanocubes are observed throughout the hydrothermal heating process of 180°C started from 4 h to 12 h. The probable growth mechanism on the formation of cubic nanostructures is also proposed. Electron micrographs show the cubic α-Fe_2O_3 synthesized at the most optimum 8 h hydrothermal heating duration are indeed produced in high-yield and with well-defined cubical shape. Typical rhombohedral structure of cubic α-Fe_2O_3 was evident by the XRD pattern. The SAED pattern indicates that the α-

Fe_2O_3 nanocubes are single-crystalline in nature, with lattice-fringes and the *d*-spacing value of 3.6 Å. The optical characterization reveals that α-Fe_2O_3 nanocubes show strong visible-light absorption with band gap energy of ~2.1 eV while the photoluminescence emission spectra depicts a mono-peak centered at ~590 nm. Both SAED pattern and UV-vis spectra show strong correlation with the standard α-Fe_2O_3. The as-synthesized α-Fe_2O_3 single crystal is high in quality that potentially to be used as a visible-light active nanomaterial in the renewable energy devices application.

Keywords: Hematite; Single crystal; Nanocubes; Hydrothermal; Characterization

1.0 Introduction

Rational design and synthesis of metal oxide nanocrystals with tunable shape and properties have attracted enormous research interest for their unique size and shape-dependent intrinsic physicochemical properties. In particular, metal oxide semiconductor nanocrystals have been identified as important materials with potential applications in a wide range of fields (optical, electrical, magnetic, catalytic, chemical, etc).[1-5] Hematite (α-Fe_2O_3) is among one of the most interesting n-type metal oxide semiconductor with optical bandgap of 2.1 eV.[6,7] Due to its prevalence, hardness, chemical- and thermal-stability, and environmentally benignity, it has become an attractive material in a spectrum of semiconducting applications. In addition, its ability to absorb light made it a particularly attractive material for use in solar energy conversion.[8,9] α-Fe_2O_3 is isostructural with corundum, Al_2O_3, which is trigonal (hexagonal scalenohedral, symbol $\bar{3}$ 2/m) with space group R$\bar{3}$c and lattice parameters a = 5.0356 Å, c = 13.7489 Å, having Fe^{3+} ions occupy 2/3 of its octahedral sites that are confined by the nearly ideal hexagonal closed-pack O lattice.[10]

The dense hexagonal close packing of oxygen combined with the interstitially positioned iron yields a very dense structure (5.26 g/cm^3) exhibiting a high polarizability and high refractive index (3.15).[11] Attributed to its layered structure also generates complex behaviour when interacting with photons and electrons, it is of interest among researchers to exploit α-Fe_2O_3 nanocrystals in numerous promising applications, such as gas sensors,[12] catalysts/photocatalysts,[13] electrode materials in lithium secondary batteries,[14] magnetic recording media,[15] photo-assisted electrolysis of water,[16] and optical and electromagnetic devices as well as environmental remediation in wastewater treatment.[17-19]

It is noted that the morphology and size of α-Fe_2O_3 have a great impact on their intrinsic physicochemical properties and thus determine their application.[20] Therefore, much effort has been made in the design of α-Fe_2O_3 materials with a desired structure and morphology such as zero-dimensional (0D) nanoparticles,[21] one-dimensional (1D) nanowires,[22] nanobelts,[23] nanorods,[24] nanotubes,[25] two-dimensional (2D) nanorings,[26] nanoflakes,[27] three-dimensional (3D) nanocubes,[28] urchin-like nanostructures,[29] nanoflowers,[30] and etc. In particular, well-defined single crystalline α-Fe_2O_3 nanocubes exposing specific facets are demonstrated to be extremely notable due to the highly reactive surfaces and excellent electron mobility.[31-33] In terms of crystallinity nature, a single crystalline α-Fe_2O_3 has a continuous crystal lattice for the entire nanostructure. The crystal lattice arrangement is endless until the edge of the atomic arrays, with no grain boundaries observed. Such continuous atomic array indeed renders several advantages especially on the aspect of its congruent electronic properties. For instance, the absence of grain boundaries in the crystal structure are found to be able to accelerate the movement of electric charges in a circuit especially in solar cells and PEC cells.[34] Additionally, single crystallinity also allows longer lifetime of electron-hole pair which could enhance the efficiency in the aforementioned applications.[35] As in the case of gas sensor application, single crystalline α-

Fe_2O_3 nanostructure is found to be able to reduce instability problems associated with grain coalescence and drift in electrical properties,[36] which alternatively improve its sensitivity and stability. Therefore, it is worth-noted that the notable characteristics can be harnessed through such structure that would enhance and diversify its performance.

To date, a myriad of chemical and physical methods has been developed for the synthesis of single crystalline α-Fe_2O_3 nanocubes. These methods include sonochemical route,[37] thermal decomposition of inorganic precursors,[38] forced hydrolysis,[39] electrospinning,[40] and hydrothermal approach.[41]. Compared with other fabrication techniques, hydrothermal synthesis is considered as the most robust method and has attracted rapidly increasing interest for the preparation of single crystalline α-Fe_2O_3 nanocubes due to several merits: the products with high purity and excellent crystallinity, morphologies easy to be tuned, relatively low reaction temperature and availableness for scale-up production. For example, Pu and co-workers have successfully synthesized α-Fe_2O_3 nanocubes by a templating method, in which they employed cationic capping agent-surfactant cetyl trimethylammonium bromide (CTAB) and showed that concentration variation of the precursor could lead to different size and shape of α-Fe_2O_3. In this study, the rod-like β-FeOOH precursors were firstly obtained by varying $FeCl_3$ concentration ranged from 0.01 to 0.05 M at 120 °C, and then the precursors aggregated into raft-like particles and thereby transformed to α-Fe_2O_3 cubic particles.[5] Mitra et al. have reported the controlled synthesis of α-Fe_2O_3 microcubic particles by pH- controlled hydrolysis of $Fe(NO_3)_3.9H_2O$ with the use of ethylenediamine as basic ligand to facilitate the formation of cubic samples,[42] whereas Su et al. used ammonium acetate in $FeCl_3.6H_2O$ aqueous solution as capping agent to produce α-Fe_2O_3 at 160 °C for 24 h.[43] In addition to this, Ma and colleagues synthesized single-crystal α-Fe_2O_3 nanocubes by the use of diethylene glycol (DEG) at 200 °C for 10 h in Li ion batteries application.[44] Very recently, Patra and his group used proportional amount of sodium salicylate and NaOH/water to successfully prepare single crystalline α-Fe_2O_3 nanocubic particles via hydrothermal route for 36 h at 423 K and investigated the facet-dependent photoredox catalytic activity.[45] However, most of the aforementioned synthetic routes tend to involve the use of organic surfactants, which means a much more complicated process including complete template removal at elevated temperature is needed. Furthermore, solvents used in either potentially hazardous or rather complicated protocol involved, and some synthesis methods are often time-consuming (>24 h). It is therefore of anticipation to further discover the growth of single crystalline α-Fe_2O_3 nanocubes and conveniently sort the particle size and desired morphology through a facile, simple, economic, and straightforward strategy in hydrothermal method.

In the experiment reported herein, driven by the demand for one pot facile hydrothermal synthesis of single crystalline α-Fe_2O_3 nanocubes with well-defined morphology and scrutinizing its size- and morphology-dependent properties, we employed the chloride-based cation Fe^{3+} that was reacted with oleate functional group in the presence of oleylamine (OAm). In the present work, it is noteworthy that: (i) Current synthetic method is very simple and straightforward. The synthetic scheme involved only one-step process that does not require high temperature or high pressure. (ii) It is particularly interesting to highlight that only the reaction time was varied in the range of 4 h to 12 h at a constant temperature, in contrast to other typical hydrothermal synthesis of 24 h or a few days. The morphological evolution of the nanostructures and their corresponding growth processes were able to be elucidated. Thereafter, detailed discussion based on the insightful analysis of the shape and structure was also presented. (iii) We account on the shape- and size- selective synthesis of single crystalline α-Fe_2O_3 nanocubes with good reproducibility without the use additional capping agent or surfactant. Instead, we have used a mixture of solvents with OAm as one of the key elements to determine the final shape of single crystalline α-Fe_2O_3 nanocubes.[46]

Previously, many experimental and theoretical studies primarily focused on the size and morphology of the α-Fe_2O_3 nanostructures.[47-49] Since α-Fe_2O_3 is a well-known visible active for its various applications. Hence, one of the most important aims of this paper was to present a study of the time-dependent morphological evolution of α-Fe_2O_3 and its transformation from 0 D to 3 D (cubic shape). Finally, the high quality single crystalline α-Fe_2O_3 nanocubes are characterized by using various analytical tools to investigate the structural- and optical-properties of α-Fe_2O_3 nanocubes in a much detailed manner. The as-obtained information is compared with that of commercial α-Fe_2O_3 nanoparticles to show the novelty of the as-synthesized product. In addition, the possible transformation mechanism of the α-Fe_2O_3 through a "1D → 3D" mode was also proposed in the following sections. The detailed crystallographic-, structural- and optical- properties of the as-prepared α-Fe_2O_3 nanocubes presented are of fundamental importance to comprehend the shape and growth of single crystallinity of α-Fe_2O_3 nanocubes and thus provide direct correlation between the shape and exposed facet-controlled properties to its application in future study.

2.0 Experimental

All the chemicals used in the experiments were of analytical grade and no further purification is required. Potassium oleate ($C_{18}H_{33}KO_2$, Sigma Aldrich, $\geq$ 87 %), ferric chloride hexahydrate ($FeCl_3.6H_2O$, Merck), Oleylamine ($C_{18}H_{35}NH_2$, Sigma Aldrich, 70%) and absolute ethanol (C_2H_5OH, HmbG Chemicals) were obtained. In this study, all the chemical reactions were carried out in deionized water.

2.1 Synthesis of α-Fe_2O_3 nanocubes

Hematite (α-Fe_2O_3) cubic nanocrystals were synthesized by using hydrothermal method. This experimental method of synthesis was carried out at the different duration and the samples were collected every 2 h. The remaining factors were kept constant while synthesizing the nanocrystals. Typically, a mixture consisting of 3.33 mmol of potassium oleate was dissolved in 5.34 mL ethanol with the addition of 1 mL oleylamine (OAm). Subsequently, the mixture was transferred into a Teflon-lined stainless steel autoclave that has been pre-loaded with 10.67 mL deionized water and 1.11 mmol of $FeCl_3.6H_2O$ aqueous solution. The resultant reagents were stirred continuously at room temperature for 2 hours until a reddish solution was formed. Then, the autoclave was sealed and hydrothermally treated at 180 °C for different heating time (4 h, 6 h, 8 h, 10 h and 12 h). After the finite induction period, the autoclave was let to cool down naturally. The resulting dark red precipitate was collected by centrifugation and washed several times with ethanol. Finally, this synthesized material was dried in the oven at the temperature of 55 °C for 24 h.

2.2 Characterizations

The size, shape, morphology, chemical composition, structural features and optical properties of the nanocrystals were investigated by using different analytical characterization techniques. We systematically observe the time-dependent morphological transformation of α-Fe_2O_3 nanocrystal structure via TEM images and SAED patterns performed by JEOL JEM-2100F that was operated at 200 kV. In order to observe the yield of α-Fe_2O_3 nanocubes in the large quantity, field-emission scanning electron microscope (FESEM, Hitachi SU8000 with the operation voltage of 2 kV) was employed. Information related to the elemental mapping and elemental composition was studied by using energy dispersive X-ray analysis (EDXA, Oxford Instrument). The bulk-crystallinity and phase identification of the samples were characterized by X-ray powder diffractometer (XRD, PANalytical EMPYREAN, 40 kV/35 mA with Cu Kα irradiation at λ= 1.5406 Å). The scanning process covered angular range from 10° to 80° with the scanning rate of 0.02° per minute. In addition, the study of phonon vibration mode was conducted by means of Renishaw inVia Raman Microscope equipped with Leica DMLM microscope (objective lens of 50x (UV)). 514 nm HeCd laser source was subjected onto the samples for 30 s at 50 mW of laser power. The spectra were collected within the range of 150 to 800 cm^{-1} by subjecting the samples to the beam source at room temperature. The X-ray photoelectron spectroscopy (XPS) measurement was performed by using synchrotron radiation from photoemission spectroscopy (PES) beamline no.3.2a at Synchrotron Light Research Institute, Thailand in order to further study the chemical elements and bonding of the single crystalline α-Fe_2O_3 nanocubes. The PES system is employed with a Thermo VG Scientific CLAM2 electron spectrometer and functioned in the conditions of maximum photon energy of 600 eV with the kinetic energy step of 1 eV for a wide scan and 0.1 eV for a narrow scan. Optical absorption spectra were analyzed by the ultra violet-near infrared spectrophotometer (UV-vis-NIR, Perkin Elmer Lamda 950). The photoluminescence (PL) spectra were obtained by using Ar^+ laser as the excitation source operated at the wavelength of 325 nm.

3.0 Results and Discussion

To acquire insight into the details of morphological evolutionary growth event and the formation of single crystalline α-Fe_2O_3 nanocubes, we have performed a time-dependent observation of the crystals growth in $FeCl_3$ solution under the hydrothermal condition at 180 °C. We have withdrawn samples out of the reaction solution at various intervals (4 h, 6 h, 8 h, 10 h, and 12 h). By then, a series of TEM images of the as-prepared samples are presented in Fig. 1a - e. Continuous formation towards the proper arrangement of α-Fe_2O_3 nanocubes from 0-D quantum dot to 3-D cubic shape was observed throughout the heating process starting from 4th h until 8th h at a constant temperature of 180 °C. At 4th hour, it is clear that a large number of quantum dots with particle size ranging from 2 to 5 nm were synthesized (Fig. 1a). Many tiny spots with a clear contrast difference in each spherical particle were acquired. A closer inspection of a selected particle reveals that the interplanar distance of 2.05 Å is belong to (202) plane of α-Fe_2O_3 as depicted in Fig. 1f. The corresponding selected area electron diffraction (SAED) rings pattern together with the intensity profile (Fig. 1k) of the spherical α-Fe_2O_3 particle also reveals a set of diffraction spots of (104), (110), (006), (024), (116) and (300) planes. As the SAED pattern can provide the internal crystal information of the whole particle, it can thus be concluded that the quantum dots are of α-Fe_2O_3 primary particles while no detectable amount of impurities has yet been produced. After 6 h, these individual particles started to undergo coalescence and spontaneously aggregate into a larger size of particle to form cluster. The corresponding d-spacing values of (012) planes obtained from different individual particles (Fig. 1g) reveals that the cluster indeed is composed of α-Fe_2O_3 primary nanoparticles by attaching intimately with each other. Thus, these interconnected particles can serve as building blocks for the transformation of nanocrystals into various shape and size during the later development. When the hydrothermal heating duration is further prolonged to 8 h, a distinctive cubic crystal with the edge length of ~ 40 nm is obtained and presented by TEM microscopic in Fig. 1c. Each individual crystal appears to be a well-defined cubical shape and it is found to be attached at the flat edges to its adjacent crystal. This preferential arrangement minimizes the total surface energy as well as surface area of as-synthesis single crystal α-Fe_2O_3 nanocubes.[50,51] The HRTEM image (Fig. 1h) and SAED pattern (Fig. 1m) of the selected region, respectively confirms the presence of α-Fe_2O_3. It is noteworthy that the diffraction

pattern of this sample displays many individual spots indicating the as-synthesized nanocubes are of highly crystalline α-Fe_2O_3. Intriguingly, with the increase of reaction time up to 10 h, the cubical shape of α-Fe_2O_3 is no longer observable and a lot of particles with the size ranging from 7 – 15 nm are started to form and the irregularity of structure can be seen in Fig. 1d. HRTEM image (Fig. 1i) and SAED pattern (Fig. 1n) display the mixture of different phases can be found in this sample. The calculated d-spacing values of 4.78 Å and 3.78 Å can be ascribed to (111) and (210) planes of maghemite (γ- Fe_2O_3). The further increment of reaction time (up to 12 h) causes the particle to undergo dissolution whereby the bigger crystals begin to deform and smaller size of nanocrystals with irregular shape are seen such as in Fig. 1e. Similarly, we found there is a presence of γ- Fe_2O_3 phase traceable through the d-spacing calculation of the selected particle in Fig. 1j and the indexed SAED pattern (Fig. 1o). The above results indicate that the morphology of α-Fe_2O_3 nanocrystals can easily be tuned and the nanocubic crystal structure is obtainable by simply adjusting the reaction time at fixed temperature in this facile one-pot procedure.

The composition and phase purity of the as-prepared samples were further elucidated by powder XRD technique. Fig. 2 shows the evolution of iron oxide phase and crystallinity changes by analyzing the α-Fe_2O_3 nanostructures that were hydrothermally treated from 4 h to 12 h (Fig. 2a – 2e). Crystalline α-Fe_2O_3 rhombohedral structures were observed at the early stage of the hydrothermal heating process of 4 h to 8 h. (JCPDS: 33-0664). It can be seen that all of the peaks can be well indexed as rhombohedral α-Fe_2O_3 (a = 5.035 Å and c = 13.747 Å) with JCPDS: 33-0664. Distinctively, the α-Fe_2O_3 nanocubes produced at 8 h show the strongest diffraction peaks at ~24.11°, 33.16° and 35.62° indicate excellent crystallinity of α-Fe_2O_3 phase produced in nanocubes. In particular, we have performed a crystallographic calculation and the formula is given in Equation 1 as below. The lattice constants obtained mainly for α-Fe_2O_3 nanocubes are a = 5.0240 Å and c = 13.7180 Å, which agrees well with the rhombohedral α-Fe_2O_3.[52]

$$\frac{1}{d^2} = \frac{4}{3}\frac{(h^2+hk+k^2)}{a^2} + \frac{l^2}{c^2} \qquad (1)$$

where d is the d-spacing of hexagonal crystal structure, a and c is the lattice constant, and (*hkl*) is the crystal plane of (012) and (104). Furthermore, if the reaction duration is increased to 10 h and 12 h (Fig. 2d and 2e, respectively), the phase of the products changes from α-Fe_2O_3 to ɣ-Fe_2O_3, which evidenced from the appearance of peaks at ~30.24° and ~ 57.19° (marked with grey dotted lines) and are in consistent with JCPDS: 39-1346 of ɣ-Fe_2O_3. These results are also in agreement with the TEM microscopic images shown in Fig. 1d – 1e, which the shape of the product turns irregular (at 10 h and 12 h).

The possible formation mechanism of the as-prepared α-Fe_2O_3 nanocubic and its morphological evolution was tentatively proposed, as shown in Fig. 3. Initially, $FeCl_3$ precursor in the reactant mixture was first hydrolyzed in the presence of water and undergoes dissolution with ethanol, producing a large number of Fe^{3+} ions (Fig. 3a). During the first 4 h, these ions nucleate into primary α-Fe_2O_3 quantum dots (Fig. 3b) attributed to the dissolution-recrystallization process and continuous growth via Ostwald ripening. The crystal growth is caused by effective coarsening at which the nucleation of particle has taken place. The chemical reactions involved in this stage can be referred as follows:[53]

$$Fe^{3+} + 3H_2O \leftrightarrow Fe(OH)_3 + 3H^+ \qquad (1)$$

$$2Fe(OH)_3 \leftrightarrow Fe_2O_3 + 3H_2O \qquad (2)$$

The OH^- anions serve as bridging agent facilitates the formation of the Fe-O-Fe skeleton. These tiny 0-D α-Fe_2O_3 quantum dots could be temporarily stabilized by oleate ions and forming coordination complexes with oleylamine (OAm). As time goes on (6th h), the OAm coordinated α-Fe_2O_3 quantum dots will subsequently grow at the expense of Fe^{3+} ions from the solution and aggregation is thus promoted. The non-aggregated quantum dots, on the other hand, will grow independently of each other, slowly consuming the smaller α-Fe_2O_3 particles. With the increase of reaction time, the size of aggregated particles will become a cluster (Fig. 3c). During this stage, it is believed that the α-Fe_2O_3 nanocrystals collided with each other and attached together by sharing a common crystallographic orientation in the initial product. This so-called topotaxial replacement[54] is the key transformation of α-Fe_2O_3 clusters into nanocuboid shape through localized conversion of single crystal into one or more nanocrystals with definite axes of symmetry. It is noteworthy that during the occurrence of this event, the fusion of α-Fe_2O_3 nanocrystal into clusters may be rationalized by lowering the surface energy along the [001] direction and thus promote the growth along the (001) plane. The following growth process from 6 h to 8 h is indeed quite interesting. Despite the growth of crystals into nanocubic system is a complicated process, for the sake of understanding the growth mechanism of nanocube, we have performed sample withdrawal taken from the oven at every two hours for postreaction characterizations via TEM technique. In the growth of nanocrystals, different facets grow at different rates. It is believed that the high-energy facets grow to a greater extent than the low- energy facets causing the nanocrystals terminated with low-energy facets. One can say that the final crystal shape is strongly dependent by the slow-growing facets and the shapes of the energy minima.[55-57] In the present study, OAm and potassium oleate were used as the capping agent to inhibit the formation of Fe-O-Fe bonds owing to the strong covalent interaction between the oleate anions and positively charged Fe^{3+} centers with some atomic configuration happen on the nanocrystal surfaces. In our case, crystal growth takes place along {102}, {112} and {012} surfaces and its equivalent direction. This means that the OAm moiety controls growth on these three facets (Fig. 3d). At this hour, the {012} facet and its equivalent surface grew to get exposed. As the duration of reaction further prolonged to 10 h, the nanocrystals of irregular shape started to form due a greater number of high energy surfaces were being exposed (Fig. 3e). As a result, there is a competition of crystal grows from different facets at the different rate causing this irregularity. We believed that some OAm by now are selectively bonded to certain crystal facet leaving the exposed facets continuous to grow. On the basis of the results shown in Fig 1i – 1j, it is also important to note that starting from 10 h to 12 h (Fig. 3e – 3f), one can observe the presence of γ-Fe_2O_3 in the samples indicating there is also phase transformation event has taken place. The transformation from α-Fe_2O_3 to γ-Fe_2O_3 has been well-studied and is governed by the nature of precursor concentration, pH, temperature, and other synthesis conditions. Phase transformation from α-Fe_2O_3 to γ-Fe_2O_3 is favoured when α-Fe_2O_3 reaches a critical size at which the combined bulk particles and surface Gibb free energy of the γ-Fe_2O_3 is greater than that of α-Fe_2O_3 particles.[61]

In order to clarify the construction of α-Fe_2O_3 nanocube, the nanocrystals obtained 8 h of the reaction process was collected and characterized in detail by electron microscopy. The representative FESEM image that was projected from the top view in order to obtain the three-dimensional nature of the α-Fe_2O_3 crystals is shown in Fig. 4a. Inset of Fig. 4a depicts only a single crystalline α-Fe_2O_3 nanocube with the edge length of ~ 40 nm. Besides, Fig 4b-4c represent the TEM images of the α-Fe_2O_3 nanocubes demonstrate that the products are all in cubic shape with no other morphology can be seen. The typical nanocubes of uniform size are seen throughout the specimen indicates high monodispersity. Each nanocube has a distinct flat-edge with average edge-length of 40 nm and the surfaces that are viewed perpendicular to the direction of incident electron beam appear to be faceted. The statistical edge length distribution is illustrated in Fig. 4b. The tendency for the formation of well-faceted nanostructures that are equilibrium in shapes is attributed to the surface energy minimization.[57] The HRTEM image shown in Fig. 4d with the lattice spacing is measured to be 0.37 nm, corresponds to (012) plane. It could be seen that these nanocubes have interfacial dihedral angle of 86°. Fig. 4e shows a fast Fourier transformation (FFT) pattern, which is obtained from the region in Fig. 4d. By examining Fig. 4e, we can also observe from the FFT that the diffraction spots are attributed to (006), $(1\bar{1}2)$, (202) and (012) lattice spots, along the [42$\bar{1}$} zone axis which is representative of the area marked with yellow square.[45] The analysis reveals the single crystalline nature of the α-Fe_2O_3 nanocrystals, having the shape of nanocuboids. Based on the above analysis, the 3D geometrical structure of the nanocube is drawn in Fig. 4f. The nanocube is enclosed by two {102}, two {012}, and two $\{1\bar{1}2\}$ exposed facets.

The SEM coupled with EDXA technique was employed to highlight the different chemical element present in the synthesized powder of α-Fe_2O_3 nanocubic structures and the results are depicted in Fig. 4g – 4j. The weight % and atomic % of constituents of the sample, respectively is shown in the table enclosed in EDXA spectrum. The presence of Fe and O components in EDXA confirms the formation of desired material. EDX analysis has also shown the presence of C and Cu peaks in addition to Fe and O peaks. The existence of C peak at ~ 0.2 keV in EDX spectrum is primarily due to the carbon tape that was used for holding the sample during the SEM and EDXA measurements. The average atomic % formation of Fe and O in α-Fe_2O_3 nanocubic structures is 38.08 % and 61.92 %, respectively. This result confirms that the O/Fe atomic % ratio of the α-Fe_2O_3 nanocubes analyzed is calculated to be 1.63, which is relatively consistent with the theoretical O/Fe atomic ratio of 1.50 for the α-Fe_2O_3. On the other hand, the elemental mapping images clearly depict that the distribution for both Fe and O is highly uniform throughout the sample.

In addition to FESEM and TEM analyses, Raman spectroscopy has been performed to give further insight into the quality and crystal phase of α-Fe_2O_3 nanocubes. It is an established, simple and most direct tool to distinguish the iron oxide polymorphs, which consist of α-Fe_2O_3, β-Fe_2O_3, γ-Fe_2O_3 and ε-Fe_2O_3; as well as other impurities.[64-66] A representative Raman spectrum of the as-synthesized single crystalline α-Fe_2O_3 nanocubes and commercial α-Fe_2O_3 is presented in Fig. 5. There are no peaks associated with any impurities can be observed. By adopting the spectral signature band of typical α-Fe_2O_3 in Table 1 to the present study, it is perceptible that the value of Raman peaks obtained for both commercial and single crystal α-Fe_2O_3 nanocubes are shifted towards lower wavenumbers. However, on the whole, one can see that the spectrum is well-correlated with commercial α-Fe_2O_3 nanoparticles reference spectrum. Typical α-Fe_2O_3 signature bands can be observed in the region of 150 to 800 cm^{-1}. Typically, there are two classes of Raman-active vibrational modes (A_{1g} modes and E_g modes) can be observed at 200 to 700 cm^{-1}, which attributed to the appearance of the major α-Fe_2O_3 characteristic within these bands.[67] The values of the spectral signature peaks that deem to be characteristic for typical α-Fe_2O_3 are presented in Table 1. Indications of the apparent spectra are as follows: Due the fact that Fe atoms are much heavier than the O atoms, peak lines between 200 and 300 cm^{-1} are of Fe atom vibrations. Meanwhile, bands between 350 to 600 cm^{-1} is due to the O atom vibrations. Further elucidations describe that A_{1g} band at 212 cm^{-1} is assigned to the movements of iron cations along c-axis while E_g mode at 384 cm^{-1} is assigned to be the symmetric breathing mode of the O atoms relative to each cation in the plane perpendicular to the crystallographic c-axis.[68] The red shift of the Raman lines for both commercial and single crystal α-Fe_2O_3 nanocubes was reported to be due to heating during the Raman scanning process.[69] Since the laser source of 514 nm was used, higher laser energy that highly focused on the surface of the samples could induce an increase in temperature. The high activation energy projected to the surface of the particles could cause dehydration that consequently increases the interfacial energy of commercial and single crystalline α-Fe_2O_3 nanocubes.

UV-vis spectrophotometry was used to study the optical absorption properties of single crystal α-Fe_2O_3 nanocubes at room temperature. Fig. 7a shows absorption spectrum of single crystal α-Fe_2O_3 nanocubes within near UV and visible region from 250 – 1100 nm. Noticeably, three peaks have been identified, which fall within the range of far UV (250 - 300 nm) and visible region (425 - 500 nm and 520 - 650 nm). In order to explain both of these absorption phenomena, a molecular orbital theory called ligand field model that describes the bonding, orbital arrangement and other characteristics of coordination complex will be employed.[72] In general, the band assignments of these absorption spectra can be made by using this ligand field theory. According to Sherman et al. (1985), it is well-established that there are three types of electronic transition inclusive of Fe^{3+} ligand field or the *d-d* transitions, pair excitation or double exciton processes and ligand to metal charge transitions (LMCT).[73] In general, the ligand field transition parameter is the orbital energy separation between two sets of Fe (*3d*) orbitals or the crystal field splitting.

As shown in Fig.7b, the region includes 250-300 nm can mainly be assigned to LMCT since the energy of the transition during the photoexcitation process is greater than 4.59 eV (λ = 270nm). At this transition energy, charge transfer may occur from the non-bonding ligand molecular orbitals (O*2p*) to the antibonding partially filled metal d-orbitals (Fe*3d*).[74] On the other hand, the second absorption region (Fig. 7c) that lies in the range of 425-500 nm can be ascribed to ligand field transitions of Fe^{3+}, which can be assigned to $^6A_1 \rightarrow {}^4E_1$, $^4A_1$ (^4G).[73] The transition of the ground state ($^6A_1$) within the crystal structure can take place with only two conditions. Firstly, the Fe^{3+} ions species must present. Secondly, there must be formation of binuclear inorganic complexes through the magnetic coupling of electronic spins of next-nearest neighbour Fe^{3+} cations. With respect to the region between 520-650 nm, the transitions are caused by 'double exciton processes' that involves strongly coupled Fe^{3+} cations rather than single Fe^{3+} cation as stated by spectroscopic selection rule.[75] The excitations of Fe^{3+}-Fe^{3+} pairs are attributed to sum of two single ion Fe^{3+} ligand field transitions that can be assigned to $^6A_1 + {}^6A_1 \rightarrow {}^4T_1 ({}^4G) + {}^4T_1 ({}^4G)$.[73] Regarding to the trend of the absorbance characteristics, the 'double exciton processes' has trigger the progressively-steep onset absorption from the wavelength of 770 nm and resulting in a strongest absorption in the region of 520 - 650 nm. The peak (571 nm) within this region is highest among three of the interband transition that being observed. Such steep absorption edge in the visible range of 580-770 nm is responsible to the reddish colour for the as-synthesized single crystal α-Fe_2O_3 nanocubes (inset of Fig 7a), which is well-complement with literature reports.[73-76] The determination of bandgap for α-Fe_2O_3 nanocubes from spectroscopic absorbance measurements $(\alpha h\nu)^{1/2}$ is plotted against the photon energy is represented in Fig. 7d. Typically, the bandgap energy was calculated from the absorbance ($\alpha h\nu$) data of α-Fe_2O_3 recorded in the wavelength range of 250 – 1100 nm using Tauc relation;

$$\alpha h\nu = A_0\,(h\nu - E_g)^n \qquad (2)$$

$$\text{where, } A_0 = \left[\frac{e^2}{nch^2 m_e^*}\right](2m_r)^{3/2} \qquad (3)$$

Here, α is the measured absorption coefficient (cm^{-1}) near the absorption edge, A_0 is a constant, $h\nu$ is photon energy (eV), Eg is optical band (eV), n is a constant. The value of n is determined from the nature of optical transition n = ½ or 2 for direct allowed and indirect allowed transition, respectively. m_e^* and m_r are the effective and reduced masses of charge carriers, respectively. The indirect bandgap energy was determined by extra-plotting the linear fit to the experimental data to zero absorbance. Hematite has an indirect bandgap and thus we have determined its indirect bandgap energies by plotting $(\alpha h\nu)^{1/2}$ versus photon energy for α-Fe_2O_3, respectively. The size of the bandgap is calculated to be ~2.1 eV, which is correlated to the literature reported value.[77-78] Fig. 7e explains the indirect transition in the parabolic nature of the bands close to the band edges of α-Fe_2O_3 pictorially. Briefly, the incoming photons (visible light) with energy in excess of the bandgap are readily absorbed, as they are likely to have enough energy to excite electrons from the band edges. For an allowed indirect bandgap semiconductor, the valence band energy peak and conduction band energy minimum occur at two different momentums. Thus, the electrons must undergo a change in momentum in addition to photon absorption in order to be fully excited into the conduction band and subsequently fall back to valence band via dissipation of energy in the form of photon.

Fig. 8 depicts the photoluminescence (PL) spectra of the nanocubes and commercial α-Fe_2O_3 nanoparticles as standard reference for comparison. Intriguingly, the nanocubes only exhibit single photoemission peak centered at around 590 nm, whereas the commercial sample displays 6 peaks (434, 468, 591, 722, 844 and 892 nm). Basically, for the small α-Fe_2O_3 nanoparticles with dimension less than 20 nm only the PL phenomenon is observable due to quantum confinement effect.[79] In contrast, bulk α-Fe_2O_3 with dimension greater than 70 nm does not exhibit prominent PL since the optical transition is forbidden.[80] In current study, the nanocubes appear to have dimension of 40 nm that lies between small and bulk size, where the effect of size still need to be considered. According to Fu et al. (2004), the sub-nanometer geometry of our nanocubes also possibly increases the Fe-O bonding separation, resulting in enhancement of the magnetic coupling of the neighbouring Fe^{3+}, which is responsible for the PL of α-Fe_2O_3 nanoparticle.[81] In the other way, the nanocubes with dimension that is greater than that of smaller nanoparticles have given smaller Racah parameters which weaken the neighboring covalency than those of smaller particles.[82] This finally led to the red shift of emission band. The single broad PL peak emitted by as-synthesized nanocubes suggested that the sample has single crystal properties, which has no grain boundaries compared to commercial α-Fe_2O_3 nanostructures.

4.0 Conclusion

The single crystal nanometer-sized rhombohedral α-Fe_2O_3 cubic particles were successfully synthesized by a facile one-pot hydrothermal method at 180 °C for several hours to study the morphological, structural and optical properties of as-synthesized sample are thoroughly. By varying the hydrothermal heating duration from 4 h to 12 h, it is concluded that the 8 h hydrothermal heating duration is the most optimum conditions for the formation of high quality single crystal α-Fe_2O_3 cubic structure. For the 8th hour of hydrothermal treatment, the as-prepared α-Fe_2O_3 comprises of numerous cubes with average edge length of 40 nm and shows characteristic of single crystal structure. The cubic formation was interpreted along the diagonal $[42\bar{1}]$ zone axis. The cubes were enclosed by {012} facet of (012), (112) and (102) planes with the angle of 86°. The existence of Fe^{3+}-oxo complexes in single crystal α-Fe_2O_3 nanocubes as was observed from Raman spectroscopy, which was not present in the commercial α-Fe_2O_3. The PL emission of single crystal α-Fe_2O_3 nanocubes confirms the single crystal characteristics with no grain boundaries. PL emission spectrum also supports the fact that cubic single crystal α-Fe_2O_3 contains Fe^{3+} ions and binuclear inorganic complexes which allowed the optical indirect transitions to occur with the existence of magnetic coupling of electronic spins of next-nearest neighbour Fe^{3+} cations in the crystal structure. The transition is thus supported by UV-vis spectrophotometry.

Acknowledgements

The financial support by Chancellory of University Malaya under High Impact Research Grant (HIR-UM) (J-21002-73810), HIR-MOHE (UM.C/625/1/HIR/MOHE/SC/06) and Flagship Project Grant (FL017-2011) are highly acknowledged. Authors also grateful for the research grants that funded by Ministry of Science, Technology and Innovation (MOSTI) (ScienceFund: 03-01-03-SF0658), Ministry of Higher Education (MOHE) (FRGS: FP-038-2014B; ERGS: ER002-2013A) and University Malaya Research Grant (UMRG: RP007B-13AFR). N.M.A. Rashid would like to specially acknowledge Postgraduate Research Fund (PG078-2014B) which is provided by Institute of Research Management and Consultancy (IPPP) University Malaya. Finally, the authors would like to acknowledge Nor Endang Arifin and Department of Physics (University Malaya) for providing analytical supports.

References

[1] X.L. Fang, C. Chen, M.S. Jin, Q. Kuang, Z.X. Xie, S.Y. Xie, R.B. Huang and Zheng, LS. *J. Mat Chem*, 2009, **19**, 6154-6160.

[2] M. Gondal, A. Hameed, Z.H. Yamani, A. Suwaiyan, *Appl Catal A – Gen*, 2004, **268**, 159-167.

[3] J.B. Joo, R. Dillon, I. Lee, Y. Yin, Bardeen C.J. and F. Zaera, *Proc. Natl. Acad. Sci.*, 2014, **111**, 7942-7947.

[4] A. Kudo and Y. Miseki, *Chem. Soc. Rev.*, 2009, **38**, 253-278.

[5] Z. Pu, M. Cao, J. Yang, K. Huang, C. Hu, *Nanotechnology*, 2006, **17**, 799.

[6] P. C. K. Vesborg and T. F. Jaramillo, *RSC Adv.*, 2012, **2**, 7933–7947.

[7] B. Sun, J. Horvat, H.S. Kim, W.S. Kim, J. Ahn, G. Wang, *J. Phys. Chem. C*, 2010, **114**, 18753-18761.

[8] Gurudayal, D. Sabba, M. H. Kumar, L. H. Wong, J. Barber, M. Grätzel and N. Mathews, *Nano Letters*, 2015, **15**, 3833-3839.

[9] S. Kumari, A. P. Singh, C. Tripathi, D. Chauhan, S. Dass, R. Shrivastav, V. Gupta, K. Sreenivas and V. R. Satsangi, *Int. J. Photoenergy*, 2007, **2007**, 1-6.

[10] J. G. Catalano, *Geochimica et Cosmochimica Acta*, 2011, **75**, 2062-2071.

[11] L. Vayssieres, J. Guo and J. Nordgren, *J. Nanosc Nanotech.*, 2001, **1**, 385-388.

[12] N. D. Cuong, T. T. Hoa, D. Q. Khieu, N. D. Hoa and N. Van Hieu, *Current App.Phy.*, 2012, **12**, 1355-1360.

[13] Y. R. Hong, Z. Liu, S. F. B. S. A. Al-Bukhari, C. J. J. Lee, D. L. Yung, D. Chi and T. S. A. Hor, *Chem. Commun.*., 2011, **47**, 10653-10655.

[14] L. Chun, X. Wu, X. Lou and Y. Zhang, *Electrochimica Acta*, 2010, **55**, 3089-3092.

[15] J. Jalli, Y.K. Hong, J.J. Lee, G. S. Abo, J.H. Park, S.G. Kim and S. C. Erwin, *IEEE Magn. Lett.*, 2010, **1**, 4500204-4500204.

[16] J. Moir, N. Soheilnia, P. O'Brien, A. Jelle, C. M. Grozea, D. Faulkner, M. G. Helander and G. A. Ozin, *ACS Nano*, 2013, **7**, 4261-4274.

[17] M. Fondell, T. J. Jacobsson, M. Boman and T. Edvinsson, *J. Mat. Chem. A*, 2014, **2**, 3352-3363.

[18] X. Guo, Y. Deng, D. Gu, R. Che and D. Zhao, *J. Mat. Chem.*, 2009, **19**, 6706-6712.

[19] Y. Yang, Y. Li, Y. Zhang and D. Liang, *Sep. Purif. Technol*, 2010, **76**, 72-78.

[20] B. Issa, I. M. Obaidat, B. A. Albiss and Y. Haik, *Int. J. Mol. Sci.*, 2013, **14**, 21266–21305.

[21] H. Xia, C. Hong, B. Li, B. Zhao, Z. Lin, M. Zheng, S. V. Savilov and S. M. Aldoshin, *Adv. Funct. Mater.*, 2015, **25**, 627-635.

[22] R. Wang, Y. Chen, Y. Fu, H. Zhang and C. Kisielowski, *J. Phys. Chem. B*, 2005, **109**, 12245-12249.

[23] P. Basnet, G. K. Larsen, R. P. Jadeja, Y.C. Hung and Y. Zhao, *ACS Appl. Mater. Interfaces*, 2013, **5**, 2085-2095.

[24] S. Lian, E. Wang, Z. Kang, Y. Bai, L. Gao, M. Jiang, C. Hu and L. Xu, *Solid State Commun.*, 2004, **129**, 485-490.

[25] T. Mushove, T. M. Breault and L. T. Thompson, *Ind. Eng. Chem. Res.*, 2015, **54**, 4285-4292.

[26] C. Jia, L. Sun, F. Luo, X. Han, L. J. Heyderman, Z. Yan, C. Yan, K. Zheng, Z. Zhang, M. Takano, N. Hayashi, M. Eltschka, M. Kläui, U. Rüdiger, T. Kasama, L. Cervera-Gontard, R. E. Dunin-Borkowski, G. Tzvetkov and J. Raabe, *J. Am. Chem. Soc.*, 2008, **130**, 16968-16977.

[27] R. Rajendran, Z. Yaakob, M. Pudukudy, M. S. A. Rahaman and K. Sopian, *J. Alloys Compd.*, 2014, **608**, 207-212

[28] T. Wang, S. Zhou, C. Zhang, J. Lian, Y. Liang and W. Yuan, *New J. Chem.*, 2014, **38**, 46-49.

[29] B. Wang, J. S. Chen and X. W. Lou, *J. Mat. Chem.*, 2012, **22**, 9466-9468.

[30] S. Zeng, K. Tang, T. Li, Z. Liang, D. Wang, Y. Wang, Y. Qi and W. Zhou, *J. Phys. Chem. C*, 2008, **112**, 4836-4843.

[31] H. Liang, X. Jiang, Z. Qi, W. Chen, Z. Wu, B. Xu, Z. Wang, J. Mi and Q. Li, *Nanoscale*, 2014, **6**, 7199-7203.

[32] Y. Zhang, S. Jiang, W. Song, P. Zhou, H. Ji, W. Ma, W. Hao, C. Chen and J. Zhao, *Energy Environ. Sci.*, 2015, **8**, 1231-1236.

[33] N. Adelstein, J. B. Neaton, M. Asta and L. C. De Jonghe, *Phys. Rev. B*, 2014, **89**, 245115.

[34] S. D. Kharade, N. B. Pawar, K. V. Khot, P. B. Patil, S. S. Mali, C. K. Hong, P. S. Patil and P. N. Bhosale, *RSC Advances*, 2016, **6**, 24985-24994.

[35] C. Liu, H. Tang, J. Li, W. Li, Y. Yang, Y. Li and Q. Chen, *RSC Advances*, 2015, **5**, 35506-35512.

[36] M. Barroso, S. R. Pendlebury, A. J. Cowan and J. R. Durrant, *Chem. Sc.*, 2013, **4**, 2724-2734.

[37] J. H. Bang and K. S. Suslick, *J. Am. Chem. Soc.*, 2007, **129**, 2242-2243.

[38] S.B. Wang, Y.L. Min and S.H. Yu, *J. Phys. Chem. C*, 2007, **111**, 3551-3554.

[39] V. Malik, B. Grobety, V. Trappe, H. Dietsch and P. Schurtenberger, *Colloids Surf. A Physicochem. Eng.*, 2014, **445**, 21-29.

[40] C. Eid, D. Luneau, V. Salles, R. Asmar, Y. Monteil, A. Khoury and A. Brioude, *J. Phys. Chem. C*, 2011, **115**, 17643-17646.

[41] M. Zhu, Y. Wang, D. Meng, X. Qin and G. Diao, *J. Phys. Chem. C*, 2012, **116**, 16276-16285.

[42] S. Mitra, D. Soumen, M. Kalyan and C. Subhadra, *Nanotechnology*, 2007, **18**, 275608.

[43] C. Su, H. Wang and X. Liu, *Cryst. Res. Technol.*, 2011, **46**, 209-214.

[44] X. Ma, M. Zhang, C. Liang, Y. Li, J. Wu and R. Che, *ACS Appl. Mat. Interf.,* 2015, **7**, 24191-24196.

[45] A. K. Patra, S. K. Kundu, A. Bhaumik and D. Kim, *Nanoscale*, 2016, **8**, 365-377.

[46] S. Mourdikoudis and L. M. Liz-Marzán, *Chem. Mat.*, 2013, **25**, 1465-1476.

[47] A. Satoh and Y. Sakuda, *Colloids Surf. A Physicochem. Eng. Aspects*, 2014, **460**, 473-482.

[48] A. Satoh, *Colloids Surf. A Physicochem. Eng. Aspects*, 2015, **483**, 341-351.

[49] P. Dias, A. Vilanova, T. Lopes, L. Andrade and A. Mendes, *Nano Energy*, 2016, **23**, 70-79.

[50] X. Feng, D. C. Sayle, Z. L. Wang, M. S. Paras, B. Santora, A. C. Sutorik, T. X. T. Sayle, Y. Yang, Y. Ding, X. Wang and Y.-S. Her, *Science*, 2006, **312**, 1504-1508.

[51] V. M. Huxter, A. Lee, S. S. Lo and G. D. Scholes, *Nano Letters*, 2009, **9**, 405-409.

[52] R. D. Rodriguez, D. Demaille, E. Lacaze, J. Jupille, C. Chaneac and J.-P. Jolivet, *J. Phys. Chem. C*, 2007, **111**, 16866-16870.

[53] P. Li, X. Yan, Z. He, J. Ji, J. Hu, G. Li, K. Lian and W. Zhang, *CrystEngComm*, 2016, **18**, 1752-1759.

[54] L. S. Dent Glasser, F. P. Glasser and H. F. W. Taylor, *Quart. Rev. Chem. Soc.*, 16, 1962, **4**, 343.

[55] Y. Xia, Y. Xiong, B. Lim and S. E. Skrabalak, *Angew. Chem. Int. Ed. Engl.*, 2009, **48**, 60-103.

[56] T. Kovačević, A. Reinhold and H. Briesen, *Cryst. Growth Des.,* 2014, **14**, 1666-1675.

[57] N.J. Bacon, M. B. Baker and B.D. Swanson, *Q.J.R. Meteorol. Soc.*, 2003, **129**, 1903–1927.

[58] W. Wu, R. Hao, F. Liu, X. Su and Y. Hou, *J. Mater. Chem. A,* 2013, **1**, 6888-6894.

[59] S. Rehman, W. Yang, F. Liu, Y. Hong, T. Wang and Y. Hou, *Inorg. Chem. Front.*, 2015, **2**, 576-583.

[60] F. Liu, J. Zhu, Y. Hou and S. Gao, *Chin. Phys. B*, 2013, **22**, 107503.

[61] S. Xiong, W. Qi, B. Huang, M. Wang and L. Wei, *J. Phys. Chem. C*, 2011, **115**, 10365-10369.

[62] L. Yu, C. Yang and Y. Hou, *Nanoscale*, 2014, **6**, 10638-10642.

[63] F. Liu, Y. Hou and S. Gao, *Chem. Soc. Rev.*, 2014, **43**, 8098-8113.

[64] M. Lübbe, A. M. Gigler, R. W. Stark and W. Moritz, *Surf. Sci.*, 2010, **604**, 679-685.

[65] M. Hanesch, *Geophys. J. Int.*, 2009, **177**, 941-948.

[66] A. M. Jubb and H. C. Allen, *ACS Appl. Mater. Interfaces*, 2010, **2**, 2804–2812.

[67] D. L. A. de Faria and F. N. Lopes, *Vib. Spectrosc*, 2007, **45**, 117-121.

[68] H. Zhu, J. Deng, J. Chen, R. Yu and X. Xing, *J. Mater. Chem. A*, 2014, **2**, 3008-3014.

[69] Y. El Mendili, J.F. Bardeau, N. Randrianantoandro, F. Grasset and J.M. Greneche, *J. Phys. Chem. C*, 2012, **116**, 23785-23792.

[70] J. Liu, H. Cao, J. Xiong and Z. Cheng, *CrystEngComm*, 2012, **14**, 5140-5144.

[71] J. D. Desai, H. M. Pathan, S.K. Min, K.D. Jung and O. S. Joo, *Appl. Surf. Sci.*, 2005, **252**, 1870-1875.

[72] P. Liao and E. A. Carter, *J. Phys. Chem. C*, 2011, **115**, 20795-20805.

[73] D.M. Sherman and T.D.Waite, *Am. Mineral.*, 1985, **70**, 1262.

[74] A.M. Jubb and H.C. Allen, *ACS Appl. Mater. & Interfaces*, 2010, **2**, 2804-2812.

[75] L. Lu, L. Li, X. Wang and G. Li, *J. Phys. Chem. B,* 2005, **109**, 17151-17156.

[76] M. Lübbe, A.M. Gigler, R.W. Stark, W. Moritz, *Surf. Sci.*, 2010, **604**, 679-685.

[77] R. H. Misho and W. A. Murad, *Sol. Energ. Mat. Sol. Cells*, 1992, **27**, 335-345.

[78] B. Tang, G. Wang, L. Zhuo, J. Ge and L. Cui, *Inorg. Chem.*, 2006, **45**, 5196-5200.

[79] L.M. Fu, Z.Y. Wu, X.C. Ai, J.P. Zhang, Y.X. Nie, S.S. Xie, G.Z. Yang, B.S. Zou, *J. Chem. Phys.*, 2004, **120**, 3406–3413.

[80] C. T. Chen and B. D. Cahan, *J. Opt. Soc. Am.*, 1981, **71**, 932-934.

[81] L. M. Fu, Z.Y. Wu, X.C. Ai, J.P. Zhang, Y.X. Nie, S.S. Xie, G.Z. Yang, B.S. Zou, *J. Chem. Phys.*, 2004, **120**, 3406–3413.

[82] L. Lu, L.P. Li, X.J. Wang, G.S. Li , *J. Phys. Chem. B*, 2005, **109**, 17151-17156.

Figure Captions

Fig. 1 Time-dependent morphological evolution growth of α-Fe_2O_3 nanocubes observed from 4th h to 12th h. (a)-(e) Low magnification view of α-Fe_2O_3 nanocrystals evolution, (f)-(j) HRTEM images of each corresponding hourly growth nanocrystals selected in (a)-(e), and (k)-(o) indexed selected area electron diffraction (SAED) patterns of each TEM view obtained from (a)-(e) together with their respective intensity profile.

Fig. 2 XRD patterns of as-synthesized α-Fe_2O_3 nanocrystal prepared at 180°C for (a) 4 h, (b) 6 h, (c) 8 h, (d) 10 h, (e) 12 h

Fig. 3 Growth mechanism of α-Fe_2O_3 nanocubes and time-dependent shape evolutionary process under hydrothermal condition at 180 °C from (a-e) 4 h - 12 h.

Fig. 4 (a) FESEM image low magnification (x100k) with nanocubic edge length histogram calculated for 142 nanocubes. Inset shows an enlarged FESEM image obtained with magnification (x800k), (b) bright field TEM image of self-assembled α-Fe_2O_3 nanocubes, (c) Single crystalline α-Fe_2O_3 nanocubes, (d) HRTEM image of selected region (yellow box marked in (c)) and the measured interplanar distance of $d_{012} = 0.37$ m with planar angle of 86° suggests rhombohedral unit cell of as-prepared α-Fe_2O_3 nanocube, (e) FFT diffraction spot generated from image (d) with zone axis $[42\bar{1}]$, (f) geometrical model of a single crystalline α-Fe_2O_3 nanocrystal with exposed facets, this nanocrystal has the shape of nanocuboid. (g) EDX spectrum, (h) Fe map, (i) O map and (j) Fe and O overlapped mixture mapping.

Fig. 5 Raman spectra of (a) single crystal α-Fe_2O_3 nanocubes and (b) commercial α-Fe_2O_3 nanoparticles as standard reference.

Fig. 6 (a) Wide scan XPS of the as-synthesized single crystalline α-Fe_2O_3 nanocubes, (b and c) high resolution XPS in the Fe3p (middle panel) and O1s (bottom panel) regions. The Fe3p and O1s regions obtained were peak-fit using Gaussian-Lorentzian components. Experimental data acquired is shown with red circle dotted markers and the red solid line represents the total calculated fit.

Fig. 7 (a) UV-visible absorption spectrum of single crystalline α-Fe_2O_3 nanocubes. Inset shows the α-Fe_2O_3 nanocubes dispersed in ethanol, narrow range spectrum that covers (b) 250 – 300 nm, (c) 300 – 800 nm, (d) Plots $(\alpha h\nu)^{1/2}$ versus optical energy obtained due to indirect transition shows the bandgap energy of ~ 2.1 eV and (e) Indirect bandgap transition of electrons upon absorption of photon energy in the visible region.

Fig. 8 Photoluminescence (PL) spectra of (a) single crystal α-Fe_2O_3 nanocubes, and (b) commercial α-Fe_2O_3 nanoparticles as standard reference.

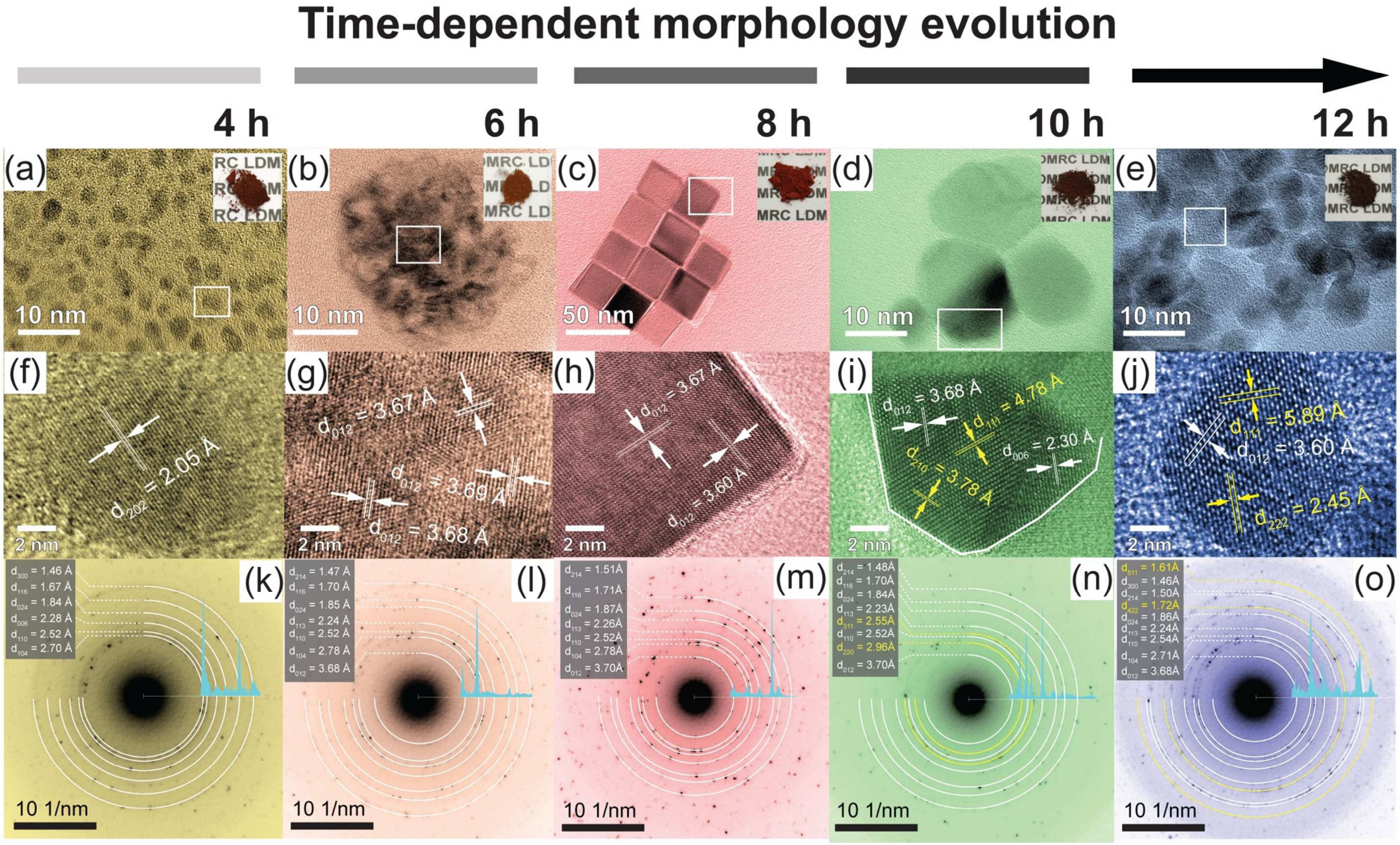

Fig. 1 Time-dependent morphological evolution growth of α-Fe_2O_3 nanocubes observed from 4th h to 12th h. (a)-(e) Low magnification view of α-Fe_2O_3 nanocrystals evolution, (f)-(j) HRTEM images of each corresponding hourly growth nanocrystals selected in (a)-(e), and (k)-(o) indexed selected area electron diffraction (SAED) patterns of each TEM view obtained from (a)-(e) together with their respective intensity profile.

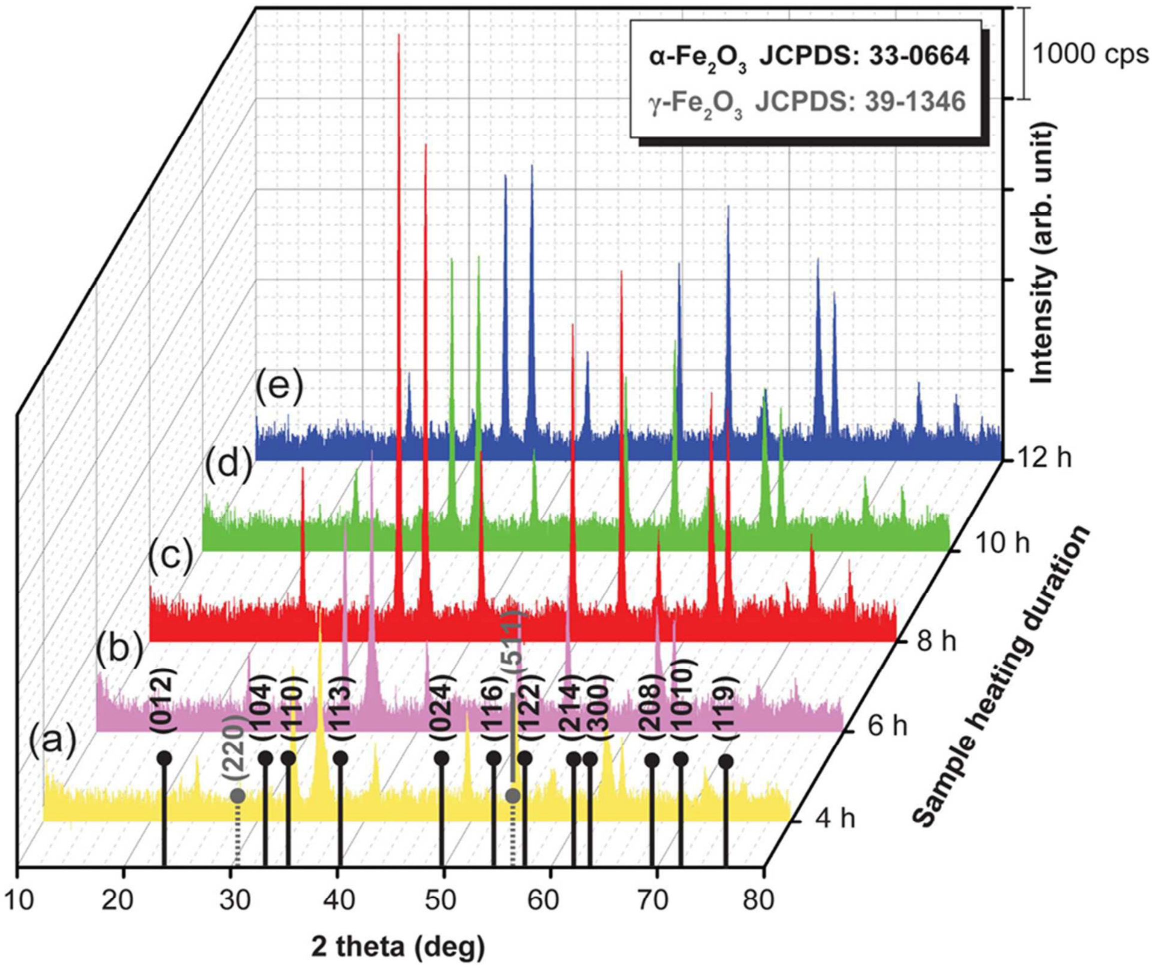

Fig. 2 XRD patterns of as-synthesized α-Fe_2O_3 nanocrystal prepared at 180°C for (a) 4 h, (b) 6 h, (c) 8 h , (d) 10 h, (e) 12 h.

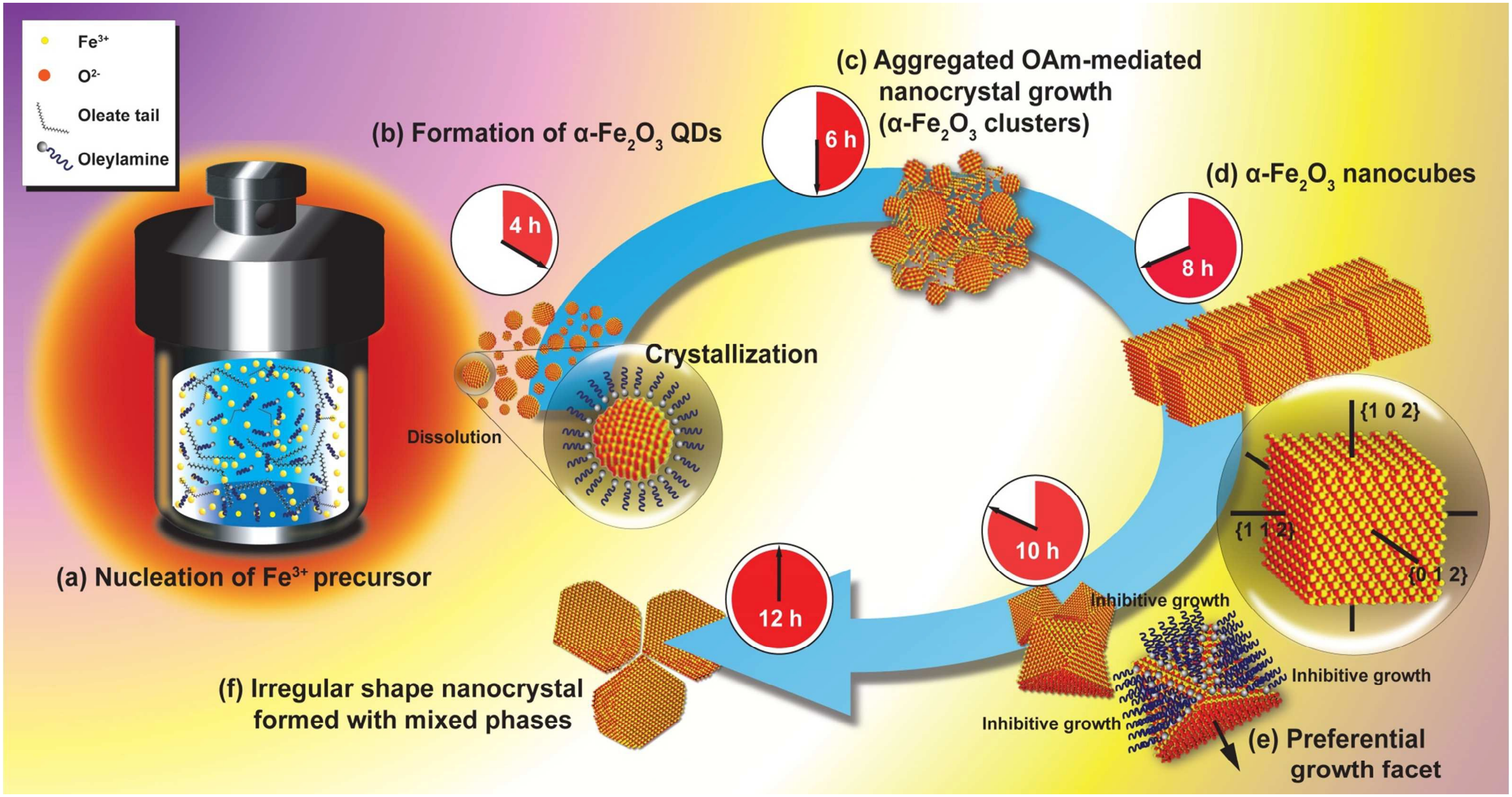

Fig. 3 Growth mechanism of α-Fe_2O_3 nanocubes and time-dependent shape evolutionary process under hydrothermal condition at 180 °C from (a) nucleation of Fe^{3+} precursor and (b-f) 4 h - 12 h.

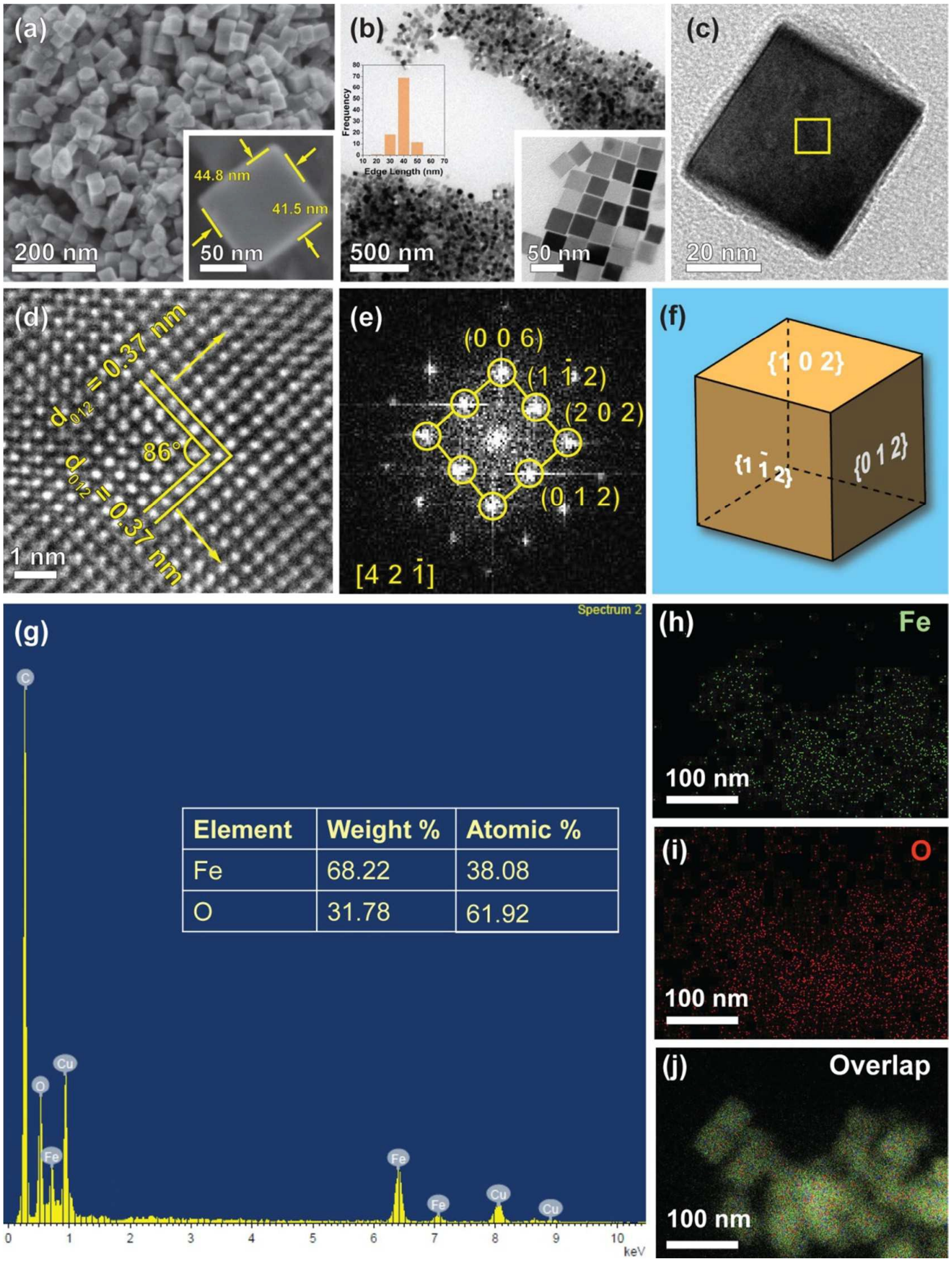

Element	Weight %	Atomic %
Fe	68.22	38.08
O	31.78	61.92

Fig. 4 (a) FESEM image low magnification (x100k) with nanocubic edge length histogram calculated for 142 nanocubes. Inset shows an enlarged FESEM image obtained with magnification (x800k), (b) bright field TEM image of self-assembled α-Fe_2O_3 nanocubes, (c) Single crystalline α-Fe_2O_3 nanocubes, (d) HRTEM image of selected region (yellow box marked in (c)) and the measured interplanar distance of d_{012} = 0.37 m with planar angle of 86° suggests rhombohedral unit cell of as-prepared α-Fe_2O_3 nanocube, (e) FFT diffraction spot generated from image (d) with zone axis [$42\bar{1}$], (f) geometrical model of a single crystalline α-Fe_2O_3 nanocrystal with exposed facets, this nanocrystal has the shape of nanocuboid. (g) EDX spectrum, (h) Fe map, (i) O map and (j) Fe and O overlapped mixture mapping.

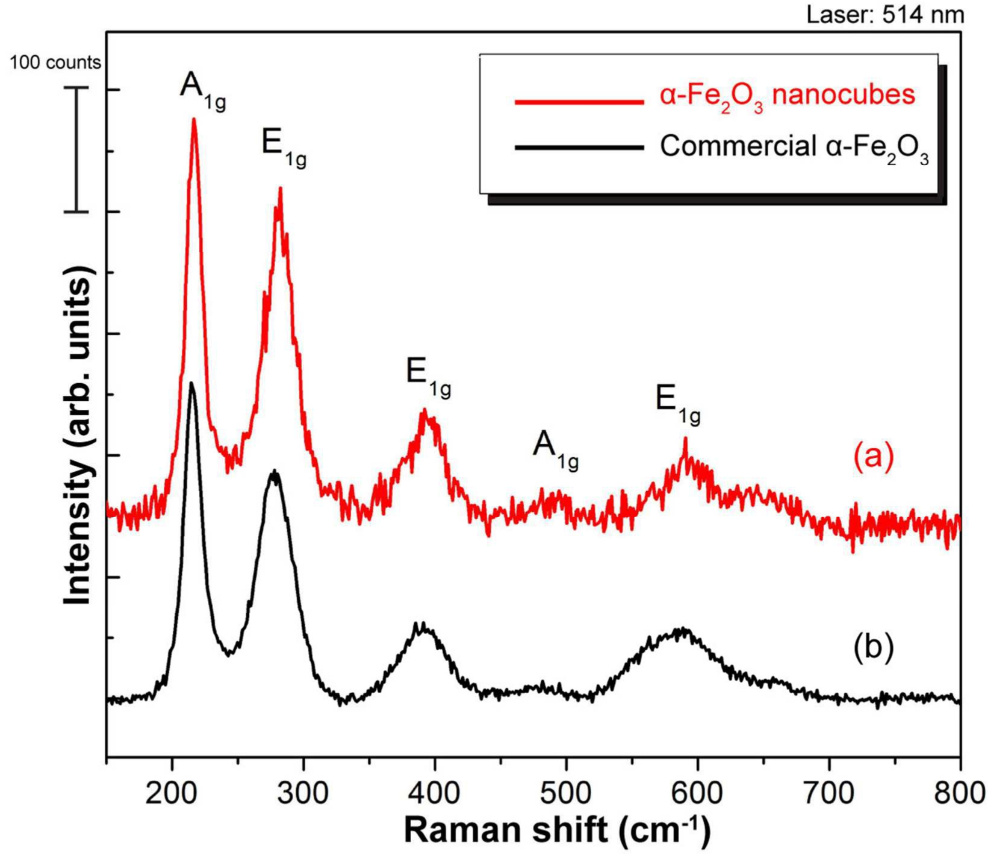

Fig. 5 Raman spectra of (a) as-synthesized single crystalline α-Fe_2O_3 nanocubes and (b) commercial α-Fe_2O_3 nanoparticles as standard reference.

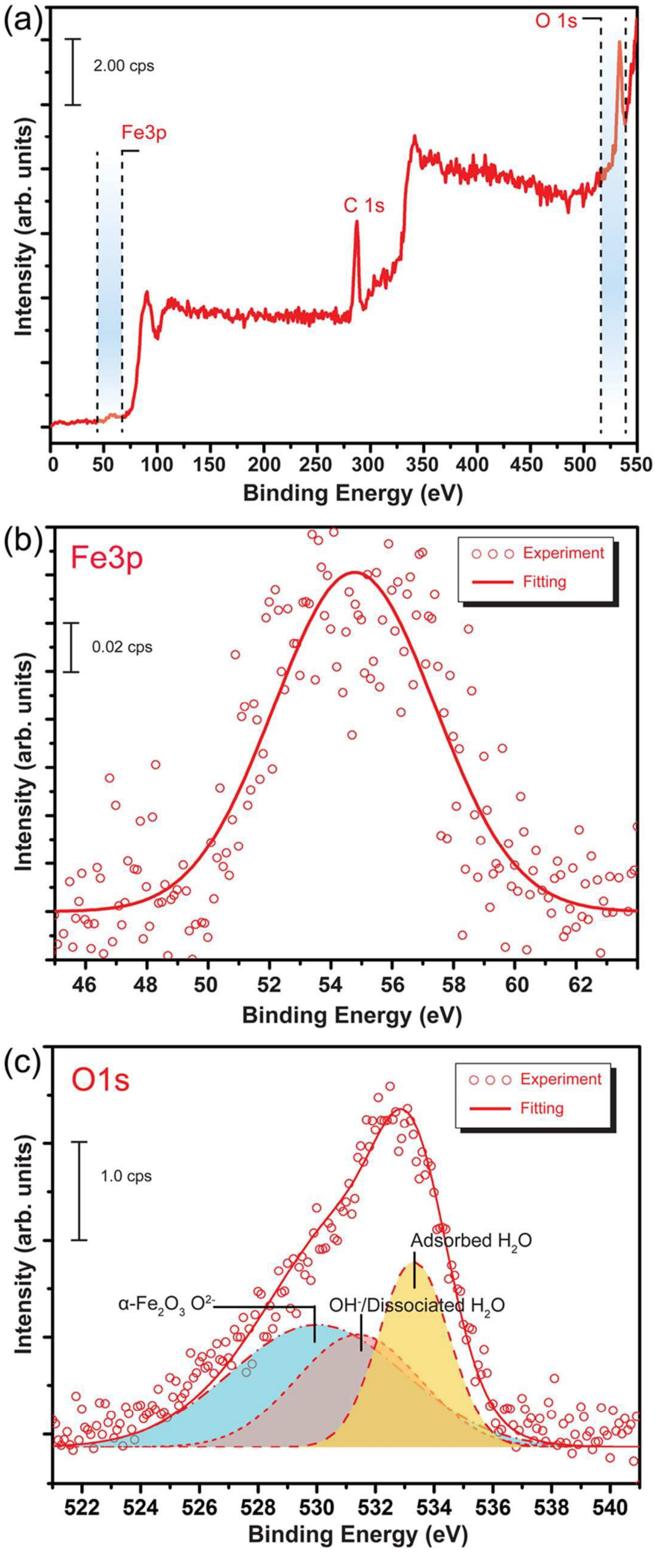

Fig. 6 (a) Wide scan XPS of the as-synthesized single crystalline α-Fe_2O_3 nanocubes, (b and c) high resolution XPS in the Fe3p (middle panel) and O1s (bottom panel) regions. The Fe3p and O1s regions obtained were peak-fit using Gaussian-Lorentzian components. Experimental data acquired is shown with red circle dotted markers and the red solid line represents the total calculated fit.

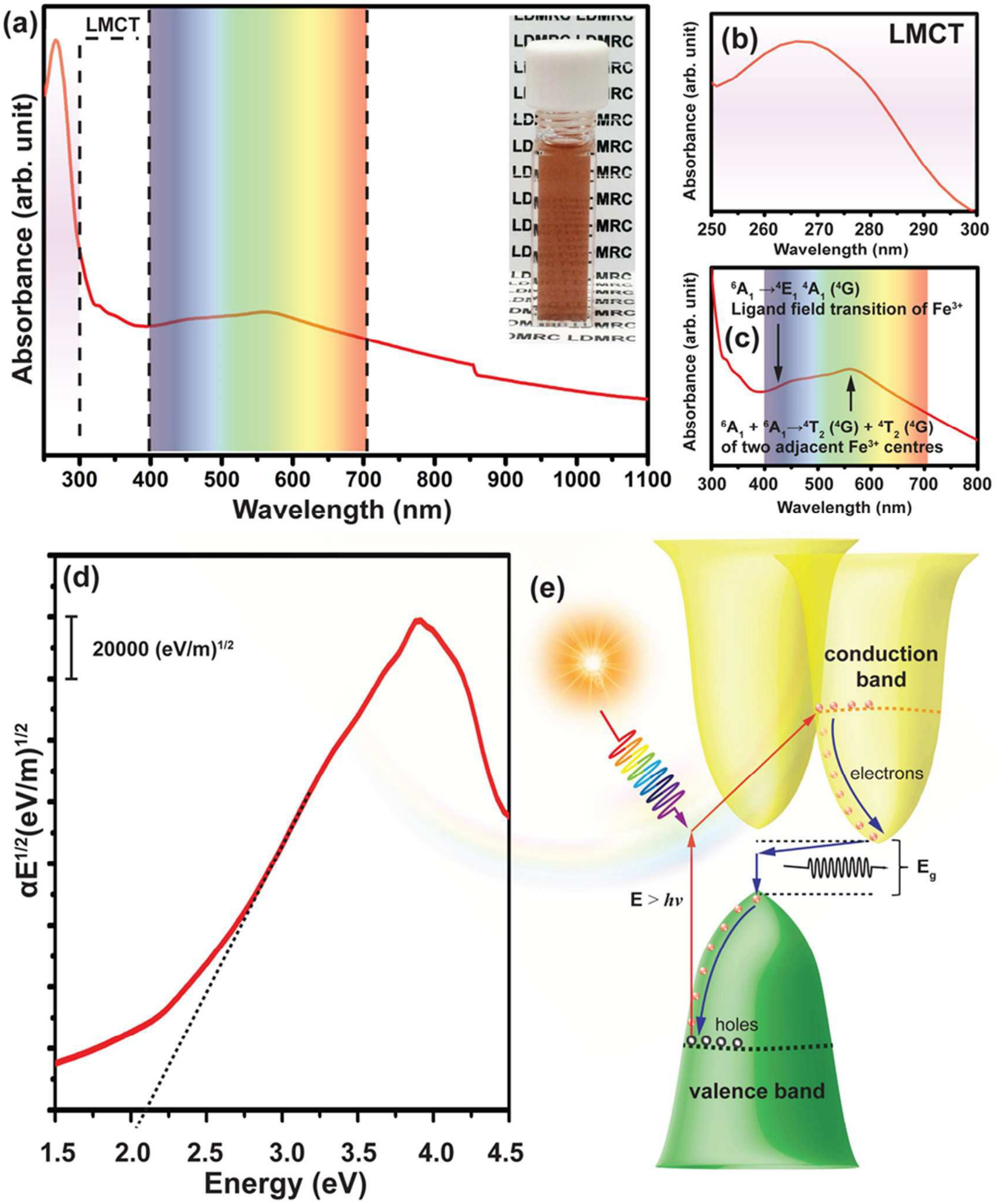

Fig. 7 (a) UV-visible absorption spectrum of single crystalline α-Fe$_2$O$_3$ nanocubes. Inset shows the α-Fe$_2$O$_3$ nanocubes dispersed in ethanol, narrow range spectrum that covers (b) 250 – 300 nm, (c) 300 – 800 nm, (d) Plots $(\alpha h\nu)^{1/2}$ versus optical energy obtained due to indirect transition shows the bandgap energy of ~ 2.1 eV and (e) Indirect bandgap transition of electrons upon absorption of photon energy in the visible region.

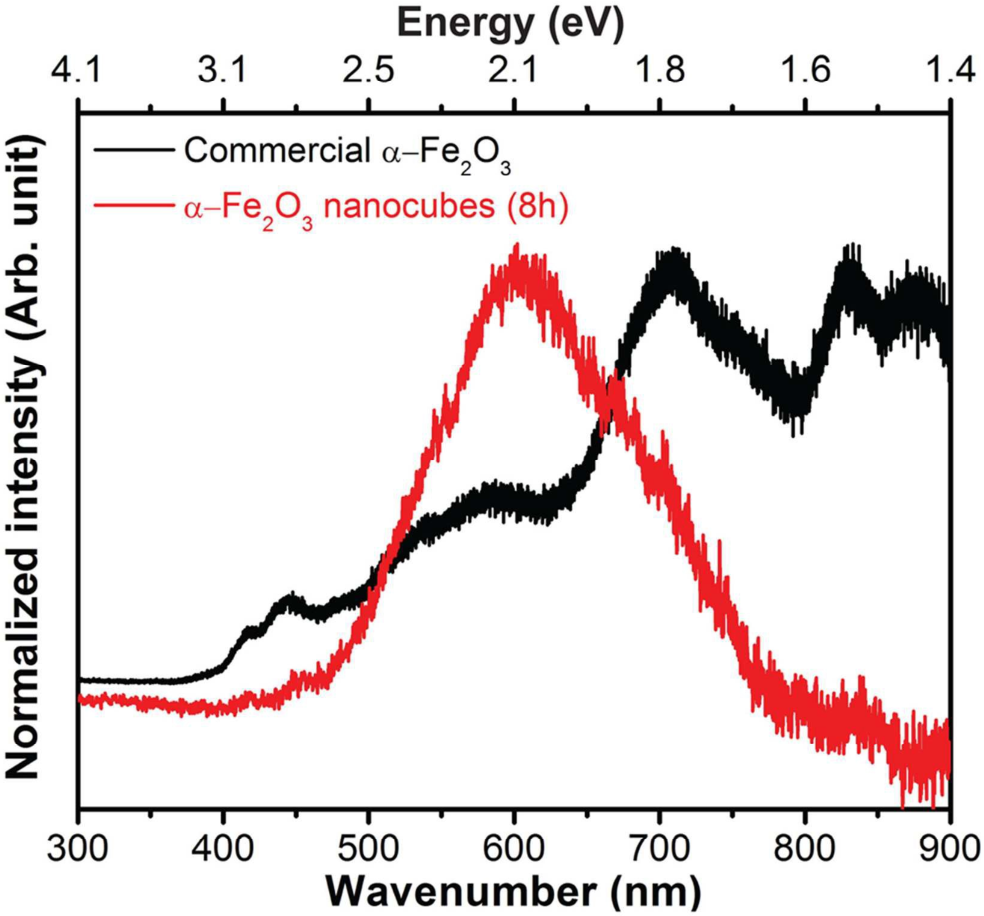

Fig. 8 Photoluminescence (PL) spectra of (a) single crystal α-Fe_2O_3 nanocubes, and (b) commercial α-Fe_2O_3 nanoparticles as reference.

Caption for table

Table 1 Band positions, corresponding intensities and assignments in the Raman spectra of typical hematite, commercial α-Fe_2O_3, and as-synthesized single crystal α-Fe_2O_3 nanocubes.

Table 1

Typical Raman shift (cm^{-1})	Raman shift of commercial α-Fe_2O_3 (cm^{-1})	Raman shift of as synthesized α-Fe_2O_3 (cm^{-1})	Assignment
225	195	212	A_{1g}
247	274	274	E_g
412	388	384	E_g
498	486	472	A_{1g}
613	591	589	E_g
824	804	800	hematite